Increasing Target Gains of Nuclear Fusion Reactors via Heavy Element ($4 \leq Z \leq 8$) Fusion

Noah Hall-King

Received March 01, 2025
Accepted June 12, 2025
Electronic access June 30, 2025

Advances made at the National Ignition Facility (NIF) have demonstrated greater than unity target gains in an inertial confinement fusion reaction. This experiment required a 2.05MJ pulse of laser light producing an output of 3.1MJ and significantly cleared the Lawson criterion. However, the energy required to power the lasers in this shot required an energy input greater than the output energy of the reaction. This posed an issue which required resolution. To solve this, two reaction cycles were composed which incorporated primordial reactions: neutron bombardments which yield heavy hydrogen (^{2}H, ^{3}H) to fuel the DT fusion accomplished in the NIF experiment. Other reactions were appended thereafter which evolve into a single or multiple CNO cycle depending on the reaction cycle. Such reactions are capable of producing energy on the order of 1.22TJ to 2.6TJ given one mole for each reaction at the observed burn-up fraction. However, issues arose when considering the 82as ($8.2 \cdot 10^{-17}$s) half-life of beryllium-8 (^{8}Be) used in the type I reaction cycle. This was resolved by modifying the reaction rates of the reactions involved. A new fuel composition has been produced that should rectify the problems in the NIF experiment N221204 by modifying reaction rates and incorporating a neutron bombardment mechanism. Increasing the rate of the seventh reaction (^{8}Be(α,γ)^{12}C) and decreasing the rate of the sixth (^{7}Be(n,γ)^{8}Be) allowed an equilibrium to be reached in the equations, further permitting ^{8}Be to be produced and consumed within six half-lives (492as) of the isotope. Conversely, a set of bridge reactions were compiled which bypass the direct consumption of ^{8}Be. Bypassing the burning of ^{8}Be, allowing the isotope to decay, and incorporating other fusion reaction of lithium and boron allow for the ignition of two distinct CNO cycles, multiplying the amount of energy produced from the type I to the type II reaction cycle by a factor of 2.13.

1 Introduction

A 2022 experiment published in 2024 by Abu-Schwareb et al. demonstrated a greater than unity target gain in an artificial nuclear reaction [1]. This inertial confinement (ICF) experiment was not capable however, of yielding sufficient energy to exceed the energy needed to power the laser array. This experiment, although successful, may be modified to produce more energy. This shortcoming may be attributed to the limitations of the experimental procedure itself, that is, the inability of the experiment to fuse elements beyond helium. Although the fuel pellet comprised a high density carbon (HDC).

By applying principles presented by Bethe on the fusion of heavy elements in heavy ($m \geq 1.3M_{\odot}$) stars [2] more exothermic processes may emerge which overcome the difference between the target gain and the energy required by the laser array. These processes, the carbon-nitrogen-oxygen cycles (the (H)CNO-I,II,III, and CNO-IV cycles depending on specifics of the star) take advantage of the reactions that occur between heavy elements ($Z \geq 6$) These reactions have larger mass defects than do light element reactions, however, they also require cumbersome energy input. This energy input can be resolved using the lighter element fusion demonstrated at NIF, as well as using a hybrid device described by Bethe in 1979 [3].By using these processes in tandem, the final hurdle before fusion unity may be cleared.

The aim of this paper is to yield insightful data on the reaction rates of a revised nuclear reaction chain, and a suitable interpretation of that data which describes the technical and engineering specifications for a hypothetical reactor which incorporates either a first stage fission reactor, and a second stage fusion reactor; or an inertial confinement reactor which can also bombard a fuel pellet with neutrons.

1.1 The Proton Proton Chain

Until now, all fusion experiments, including the N221204 shot at NIF [1], have only achieved reaction of the the proton-proton chain (pp-chain). The trouble with this: the limited mass excess of the reactions of hydrogen into helium. These reactions predominately occur between isotopes and isomers of hydrogen and helium, and were discovered by Eddington in 1920 [4]. All of the chains begin with the fusion of protons to form deuterium (D, ^{2}H, etc.). From there, it is bombarded again by protons to yield helium 3 (^{3}He). Photons are also produced throughout these reactions to preserve mass and energy across the reactants and products. Photon production is also common across the

prelimenary reactions as well as all four branches. After this, the reactions branch into one of four chains, and are numbered accordingly.

1.1.1 *Branches of the pp-Chain*

1. **Branch I.** In this case, the ^{3}He fuses with an identical nucleus to yield an alpha particle (^{4}He, α) and two additional protons. Photons are also produced throughout these reactions to preserve mass and energy across the

2. **Branch II.** This branch fuses ^{3}He with an alpha particle (which could originate in the branch I or IV reaction). This fusion produces beryllium 7 (^{7}Be). Via electron absorption, ^{7}Be becomes lithium 7 (^{7}Li). This then fuses with a proton to produce two alpha particles. This branch, as well as I and IV produce alpha particles, however, in different proportions and with other products as well.

3. **Branch III.** This branch bares similarity to the former in that it begins with the fusion of ^{3}He and ^{4}He to produce ^{7}Be. However, it diverges as ^{7}Be is bombarded with protons to yield ^{8}B. This rapidly decays into beryllium 8 (^{8}Be) via the β^+ decay mode, which again decays into two alpha particles.

4. **Branch IV.** This branch is similar to the first one, except it fuses ^{3}He with a proton to produce an alpha particle. Quantum properties like spin and charge are preserved in this case through the production of positrons (e^+, or β^+) and electron neutrinos.

1.2 The Triple Alpha Process

The triple alpha process is a set of nuclear reactions which occurs following the completion of a pp-chain and is responsible for the production of the intermediate elements between the pp-chain and the CNO cycle. In this case, ^{4}He fuses with itself and yields ^{8}Be, similarly to the third branch of the pp-chain. This rapidly fuses with another α particle to yield carbon 12 (^{12}C). Depending upon the conditions of the star, it may proceed into the CNO cycle.

1.3 Incorporation of the CNO cycle

The carbon-nitrogen-oxygen (CNO) cycle is a positive feedback loop of reactants which cycles through stages of carbon, nitrogen, or oxygen. The process comes in three varieties (CNO-I,II,III,IV) and four hot varieties (HCNO-I,II,III). These were discovered over the course of many years by Bethe[3] and Weizscker[5,6]. It must be subsequent to a triple alpha process to provide the lightest elements of the processes.

1.3.1 *The CNO Cycles*

1. **CNO-I.** The CNO-I cycle begins with the production of carbon 12 (^{12}C), which takes place in a preceding reaction chain. ^{12}C fuses with protium (^{1}H, p, or other symbol for the proton) yeilding nitrogen 13 (^{13}N). ^{13}N decays very briefly via β^+ decay, and forms carbon 13 (^{13}C). ^{13}C fuses again with ^{1}H to yield nitrogen 14 (^{14}N). Finally, ^{14}N fuses with ^{1}H, yielding oxygen 15 (^{15}O). This again decays rapidly into ^{15}N, which fuses with ^{1}H, producing ^{4}He, and ^{12}C, which closes the loop. For reactions that produce stable isotopes, photons are produced to account for the mass deficit between products and reactants. It can also be shown in shorthand as $^{12}\text{C}\rightarrow^{13}\text{N}\rightarrow^{13}\text{C}\rightarrow^{14}\text{N}\rightarrow^{15}\text{O}\rightarrow^{15}\text{N}\rightarrow^{12}\text{C}$.

2. **CNO-II.** The CNO-II cycle begins in a different manner: with nitrogen 15 (^{15}N); again, this isotope is assumed to be first produced in another cycle*. ^{15}N fuses with ^{1}H to produce oxygen 16 (^{16}O). ^{16}O fuses with ^{1}H to produce fluorine 17 (^{17}F). This decays via the β^+ mode into oxygen 17 (^{17}O). ^{17}O fuses with ^{1}H, to produce ^{14}N and ^{4}He. ^{14}N fuses with ^{1}H to produce ^{15}O, which in turn decays back into ^{15}N to re-initiate the process. Again in shorthand, $^{15}\text{N}\rightarrow^{16}\text{O}\rightarrow^{17}\text{F}\rightarrow^{17}\text{O}\rightarrow^{14}\text{N}\rightarrow^{15}\text{O}\rightarrow^{15}\text{N}$.

3. **CNO-III.** This variation of the cycle begins with ^{17}O fusing with ^{1}H, producing fluorine 18 (^{18}F). ^{18}F decays into oxygen 18 (^{18}O). This fuses with ^{1}H, yielding ^{4}He and ^{15}N. This fuses with ^{1}H again to return to oxygen: ^{16}O. This fuses to produce ^{17}F, which decays back into the original isotope completing the loop. the shorthand of this process is: $^{17}\text{O}\rightarrow^{18}\text{F}\rightarrow^{18}\text{O}\rightarrow^{15}\text{N}\rightarrow^{16}\text{O}\rightarrow^{17}\text{F}\rightarrow^{17}\text{O}$.

4. **CNO-IV.** This type begins similar to the CNO-III cycle, as it begins with oxygen. ^{18}O fuses to yield fluorine 19 (^{19}F). This fuses with ^{1}H to produce ^{4}He and ^{16}O. Fusion again yields fluorine–^{17}F–which soon decays into ^{17}O via β^+ decay. ^{17}O fuses with ^{1}H, producing ^{18}F, again decaying via β^+ emission into ^{18}O, thus closing the loop. In shorthand, $^{18}\text{O}\rightarrow^{19}\text{F}\rightarrow^{16}\text{O}\rightarrow^{17}\text{F}\rightarrow^{17}\text{O}\rightarrow^{18}\text{F}\rightarrow^{18}\text{O}$.

1.3.2 *The HCNO Cycles*

In cases of extreme temperature and pressure, the rate of proton consumption exceeds that of the rate of β^+ decay. Because of this, similar yet distinct reaction cycles arise which include fewer decay stages, often due to longer half lives of the species.

1. **HCNO-I.** The HCNO-I cycle is similar to the CNO-I cycle as it begins with the bombardment of ^{12}C with protons. In the next step, instead of decaying, ^{13}N absorbs a proton, forming oxygen 14 (^{14}O). ^{14}O then decays into ^{14}N, which fuses back into ^{15}O. This decays again into nitrogen (^{15}N) via β^+ emission. ^{15}N again fuses to form

* As are the initial reactants in all of the CNO cycles.

^{4}He and ^{12}C which closes the loop. In shorthand this is, ^{12}C$\rightarrow^{13}$N$\rightarrow^{14}$O$\rightarrow^{14}$N$\rightarrow^{15}$O$\rightarrow^{15}$N$\rightarrow^{12}$C.

2. **HCNO-II.** This parallels the CNO-II cycle, beginning with ^{15}N. This forms ^{16}O. ^{16}O fuses to form ^{17}F, which does not decay, instead fusing into neon 18 (^{18}Ne). Through β^+ emission, ^{18}F returns to fuse into ^{4}He, and ^{15}N, thus closing the loop. Shorthand: ^{15}N$\rightarrow^{16}$O$\rightarrow^{17}$F$\rightarrow^{18}$Ne$\rightarrow^{18}$F$\rightarrow^{15}$N

3. **HCNO-III.** This mechanism resembles an extension of the HCNO-II cycle, rather than a condensed version of a CNO cycle. It begins with ^{18}F as it fuses to produce neon 19 (^{19}Ne). This decays back into fluorine (^{19}F) which fuses to emmit an alpha particle and ^{16}O. This again returns to fluorine (^{17}F), which fuses into ^{18}Ne, which decays back into ^{18}F via β^+ decay, thus closing the loop. In sort, ^{18}F$\rightarrow^{19}$Ne$\rightarrow^{19}$F$\rightarrow^{16}$O$\rightarrow^{17}$F$\rightarrow^{18}$Ne$\rightarrow^{18}$F.

1.4 Cycle Transitions

Literature discussing the transitions between the pp-chain and triple alpha process, as well as from the triple alpha process to the CNO cycle, has been published in a number of reviews, among those the Borexino collaboration[7] and Adelberger[8]. In total, these papers describe means of preliminary fusion reactions that are required to begin other fusion cycles.

1.4.1 Proton-Proton to Triple Alpha Transition

This transition occurs either as a direct transmission of alpha particles from the end of any of the branches, directly into the beginning of the triple alpha process[8,9]. This is a relatively simple approach, and is generally what occurs in less dense stars, where internal pressure is lower[8–10].

Conversely, other jumps may occur which leap directly from branch III to the triple alpha process. This occurs as a result of the overlap of the two reaction cycles[10]. By interrupting the sequence of reaction during the beryllium step: direct fusion of ^{8}Be with ^{4}He. Doing so completes the triple alpha process and provides another mechanism for transitioning between the pp-chain and the triple alpha process.

1.4.2 Triple Alpha to CNO transition

Regardless of type, all CNO cycles must begin as a CNO-I cycle[8]. However, depending on the nature of the star, it may be able to break the cycle branching off to form cascading CNO-II,III, and IV cycles. Thus, the transition occurs when a ^{12}C nucleus from a triple alpha process is bombarded with protons. Once this occurs at a great enough frequency, interruptions can occur, moving the cycle from CNO-I to CNO-II. Again, given specific conditions inside a star[10], decay of ^{15}N may be bypassed. Doing so ignites a CNO-II cycle, as the process repeats itself for the CNO-III to CNO-IV transition.

2 Methods

The aim of this paper is to yield technical data via theoretical methods. This theoretical framework will incorporate work by Einstein on the energy of quantum particles[11], and therefore, the q-value of a nuclear reaction (i.e. the energy released by each of the reactions). Further contribution from Clayton, describe the cross sections of nuclear reactions, as well as nuclear reaction rates[12]. Because of the tedious nature of the computations involved, much of the calculation was done using numerous python applications[7] (a full documentation of the code can be found in Appendix A). This was not a matter of necessity as the computations of q-value could have been done by hand, however, because of the greater computational complexity of the cross section and other data, the process was automated to avoid human error and save time.

The data yielded by the investigation of the q-values, cross sections, reaction rates, and Lawson criteria were used to determine optimal reaction cycles for nuclear fusion reactors which were used to substantiate the efficacy of the reaction cycles composed.

2.1 Computation of the Q-value

As discussed above, Einsteins special relativity equation[11] may be used to describe the q-value of the reaction. This has been a primary application of the discovery, dating back to Meitner's fission experiment, and the Manhattan project. To compute the energy evolved or absorbed by a reaction, the energies of the incident and output particles are computed, and their difference taken. To do this, the particles are said to have constant velocity before and after the reactions. This velocity is furthermore set to 0 at the instant it is produced. this allows for the momentum terms of the momentum-energy relation to resolve to 0.

$$E^2 = pc^2 + (m_0c^2)^2 = (m_0c^2)^2 \Rightarrow E = m_0c^2 \tag{1}$$

where m_0 is the intrinsic rest mass of the particle in question. This further yields the energy change definition of the q-value.

$$Q = \Delta E = m_ic^2 - m_fc^2 \tag{2}$$

Finally, this equation collapses into a final form,

$$Q = c^2\Delta m \tag{3}$$

in which Δm is simply the difference in mass between product and reactant.

2.2 Nuclear Cross Section

The nuclear cross section is the quantity which describes the likelihood of a nuclear reaction. This is the nuclear analog for

the Gibbs free energy in chemistry. This quantity can be computed using the equation described by Clayton[12]. The equation used for this evaluation is shown in Eq. 4.

$$\sigma = \pi \frac{\lambda^2}{4\pi^2} \rho P_l(\rho, \eta) X(Q,A) \tag{4}$$

Where μ is the de Broglie wavelength, μ is the mass defect, v is the reaction velocity, ρ is the radius dependence of the reaction, and η is the charge dependence of the reaction (a full demonstration of all derivations can be found in Appendix B). $P(\rho,\eta)$ is the penetration factor of the reaction, and describes the wave functions of the incident nuclei. $X(E,A)$ is the similarity factor of the reactants. This expression is a simplification of a much more convoluted equation.

2.2.1 Area Factor

This area factor is the area subtended by the de Broglie wavelength of the wave function which describes the reaction. This value is related to the fundamental values of this procedure in Eq. 5.

$$\frac{\lambda^2}{4\pi^2} = \frac{\hbar^2}{(\mu v)^2} \tag{5}$$

Where $\hbar$ is the modified Planck constant ($6.626 \cdot 10^{-34}$ J·s).

2.2.2 Penetration Factor

The penetration factor describes the interaction of the wave functions of the incident particles. This factor is expressed in terms of the regular and irregular coulomb wave functions demonstrated in Eq. 6.

$$\rho P_\ell(\eta,\rho) = \frac{\rho}{F_\ell^2(\eta,\rho) + G_\ell^2(\eta,\rho)} \tag{6}$$

The regular and irregular coulomb wave functions are demonstrated in Eq. 7-9

$$F_\ell(\eta,\rho) = \frac{1}{2i}\big(H_\ell^{(+)}(\eta,\rho) - H_\ell^{(-)}(\eta,\rho)\big) \tag{7}$$

$$G_\ell(\eta,\rho) = \frac{1}{2}\big(H_\ell^{(+)}(\eta,\rho) + H_\ell^{(-)}(\eta,\rho)\big) \tag{8}$$

$$\begin{aligned} H_\ell^{(\pm)}(\eta,\rho) = {} & \mp 2i(-2)^\ell \exp\Big(\frac{\pi\eta}{2} \pm i(\sigma_\ell + \rho) + \ell + 1\Big) \\ & \times U(\ell + 1 \pm i\eta, 2\ell + 1, \mp 2i\rho) \end{aligned} \tag{9}$$

Where U is the Tricomi function, and is further expressed fundamentally in terms of the Kummer function, M in Eqs. 10, 11.

$$\begin{aligned} U(x,y,z) = {} & \frac{\Gamma(1-y)}{\Gamma(x+1-y)} M(x,y,z) \\ & + \frac{\Gamma(y-1)}{\Gamma(x)} z^{1-y} M(x+1-y, 2-y, z) \end{aligned} \tag{10}$$

$$M(x,y,z) = \sum_{n=0}^{\infty} \frac{x^{(n)} z^n}{y^{(n)} n!} \tag{11}$$

Where $a^{(n)}$ is the rising factorial s.t. $a^{(0)} := 1$ and $a^{(n)} = a(a+1)(a+2)\cdots(a+n-1)$

2.2.3 Similarity Factor

The similarity factor $X(E,A)$ is represented by the expression in Eq. 12.

$$X(Q,A) \propto \exp\Big(-\frac{B_C}{\sqrt{Q}}\Big) \tag{12}$$

Where B_C is the height of the coulomb barrier, and is rephrased in more detail in Eq. 13.

$$X(Q,A) \propto \exp\Big(\frac{kZ_I Z_j e^2}{R_I \sqrt{Q}}\Big) \tag{13}$$

Where k is coulombs constant ($k = 9 \cdot 10^9$ N·m^2/C^2), Z_I and Z_j are the atomic number of the target and projectile nuclei respectively, e is the elementary charge ($e = 1.60 \cdot 10^{-19}$C), and R_I is the radius of the target nucleus. Because of the exponentiation of the terms, $X(E,A)$ is treated as a dimensionless constant because of the nature of the exponential function (i.e. the tendency for the units to diverge to infinity in the Taylor expansion of the exponential). This proportionality allows for the derivation of Eq. 14 which describes the coefficient on the exponential term.

$$X(Q,A) = S(A) \exp\Big(-\frac{kZ_I Z_j e^2}{R_I \sqrt{Q}}\Big) = r_0\Big(A_I^{\frac{1}{3}} + A_j^{\frac{1}{3}}\Big) \exp\Big(-\frac{kZ_I Z_j e^2}{R_I \sqrt{Q}}\Big) \tag{14}$$

Where r_0 is the nuclear radius constant ($r_0 = 1.2$ fm), and A is the nuclear mass number of the nucleus.

2.3 Rate of Nuclear Reaction

This is the crux of the type I reaction cycle. The purpose conducting this investigation is to yield differential equations which describe the reaction rates. These forms were outlined by Clayton[12], and is shown below in Eq. 15.

$$\frac{dn_I}{dt} = \dot{n}_I = -n_I n_j \langle \sigma_{Ij} v \rangle \tag{15}$$

Where $\dot{n}_I$ is the rate of change of the number density of I with respect to time, n_I and n_j represent the number of moles of each reactant, and $\langle \sigma_{Ij} v \rangle$ is a suitable average of the nuclear cross section times the velocity of the reaction.

This value, in tandem with the q-value of reaction give critical insights into the efficiency of a nuclear reactor. Future reactors which gather experimental data on volume of reactant versus power output can be used as a performace metric of the reactor. (*see Discussion*)

2.3.1 The $n_I(t)$ and $n_j(t)$ Functions

The $n_I(t)$ and $n_j(t)$ functions represent the number densities of the reactants at any given time t. This number density is a scalar value, and furthermore, the functions are represented as the differential equation describing production integrated from time $t = 0$ to $t = t$, that is, $n_I(t) = \int_{[0,t]} \dot{n}_k dt$. For an example in which the reaction transition from T(D,n)α to $\alpha(^3\text{He},\gamma)^7\text{Be}$ have reaction rates shown in Eq. 16.

$$\frac{dn_I(^3\text{He})}{dt} = \langle \sigma_{Ij} v \rangle \int_{[0,t]} \frac{dn_I(\text{T})}{dt} dt \int_{[0,t]} \frac{dn_k(^3\text{He})}{dt} dt \tag{16}$$

This phenomena arises as the production rate of alpha particles is equivalent to the consumption rate of tritium.

2.3.2 Cross Section-Velocity Average

This average arises from the Maxwell-Boltzmann distribution of probability states as a function of particle velocities. The formula for this average is in Eq. 17.

$$\begin{aligned} \langle \sigma_{Ij} v \rangle &= \sqrt{\frac{8}{(Tk_B)^3 \pi \mu}} \int_0^\infty \sigma_{Ij} Q \exp\left(-\frac{Q}{k_B T}\right) dQ \\ &= \frac{2\sigma_{Ij}}{(k_B T)^2} \sqrt{\frac{2}{(Tk_B)^3 \pi \mu}} \end{aligned} \tag{17}$$

Where T is the temperature of the reaction, k_B is the Boltzmann constant ($k_B = 1.38 \cdot 10^{-23}\text{J/K}$).

The temperature of the individual particles was computed using the kinetic energy of individual particles, based on the root-mean-square speed[13] of the particles (*see Eq. 18*).

$$\tilde{E} = \frac{3}{2} k_B T = \frac{1}{2} \mu v^2 \tag{18}$$

Rearranging this equation, temperature of the a specific reaction can be found using Eq. 19.

$$T = \frac{1}{3k_B} \mu v^2 \tag{19}$$

Where v maximizes the value of the Maxwell-Boltzmann distribution. This velocity distribution is in Eq. 20.

$$f(v) = 4\pi v^3 \sqrt{\left(\frac{\mu}{2\pi k_B T}\right)^3} \exp\left(-\frac{\mu v^2}{2k_B T}\right) \tag{20}$$

In this equation, temperature T is approximated to $3.63 \cdot 10^6$K: the temperature achieved in the NIF experiment[?] however, this is different from the temperature derived in Eq. 18: the specific temperature of the reaction. From this, a final consumption rate function was composed in Eq. 21.

$$\frac{dn_I}{dt} = \dot{n}_I = -n_I n_j \frac{2\sigma_{Ij}}{(k_B T)^2} \sqrt{\frac{2}{(Tk_B)^3 \pi \mu}} \tag{21}$$

2.4 The Gamow Peak

Above we described mathematical modeling of the average temperatures of the particles using the Maxwell-Boltzmann distribution[13]. This function is a probability distribution (PDF) of all particles that are traveling at velocity v. In addition to this and the nuclear cross section, the Gamow factor provides critical insight into the probability of two nuclei to overcome the coulomb barrier. For nuclear fusion, this formula is given in the equation:

$$P(E) = \exp\left(-\frac{E}{k_B T} - \sqrt{\frac{E_G}{E}}\right) \tag{22}$$

where α is the fine structure constant, and $E_G = 2\mu c^2 (\pi \alpha Z_I Z_j)^2$ is the Gamow energy[14]. This in all defines a PDF of a reaction occurring for particles with energy E. Taking the derivative with respect to energy we are left with

$$P'(E) = \left(\frac{E_G}{2\sqrt{E_G E^3}} - \frac{1}{k_B T}\right) \exp\left(-\frac{E}{k_B T} - \sqrt{\frac{E_G}{E}}\right) \tag{23}$$

Setting this function to 0 and solving for E, a peak is discovered at $E = \left(E_G \left(\frac{k_B T}{2}\right)^2\right)^{1/3}$. At this particle energy, the reaction is most likely to occur. By further solving for velocity, the particle velocity at which the reaction is most likely to occur may be found:

$$v_{\text{rxn}} = \sqrt{2\mu \left(E_G \left(\frac{k_B T}{2}\right)^2\right)^{1/3}} \tag{24}$$

3 Results

3.1 Derived Reaction Cycles

3.1.1 Type I

From the data gathered via the methods described above, the first reaction chain composed began with the neutron bombardment of hydrogen to yield tritium and deuterium. This yield allows for the start of DD and DT fusion, which yields neutrons and isotopes of helium (^{3}He and ^{4}He respectively). These isotopes then pass through stages of the triple alpha process to achieve CNO fusion, which sustains itself given a steady stream of hydrogen nuclei. Thus, a reaction process was producedthis will henceforth be referred to as the type I reaction cycle, and is illustrated in figure 1. This process is, however, limited in it efficiency due to the loss of ^{8}Be consumed in the seventh reaction. Thus, a revised version of this process was composed as an alternative to this chain. Conversely, optimization of the reaction rate of these reactions could also allow for them to occur inside an ideal reactor.

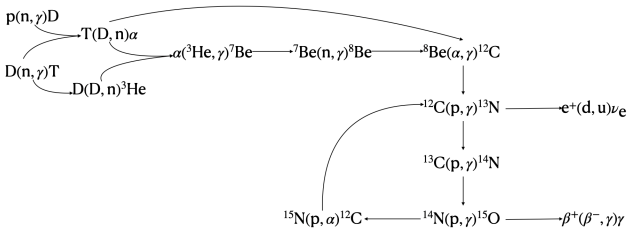

Fig. 1 *Reaction cycle proposed which directly consumes ^{8}Be to produce ^{12}C which initiates the CNO cycle. Original work of the author.*

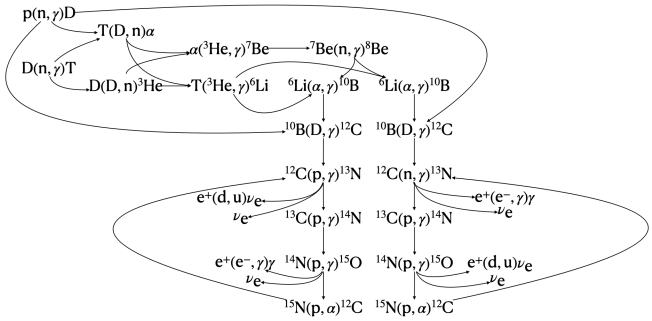

Fig. 2 *The reactions proceed in similar manners, and initiates distinct CNO cycles. The alpha particles produced in the last part of the CNO cycles are used to initiate chain reactions of ^{10}B production. Original work of the author.*

3.1.2 Type II

As discussed above, the consumption rate optimized reaction chain contained a critical flaw: the consumption of ^{8}Be within the attosecond half-life of the nuclide. Although possible through a deficit of ^{8}Be within the reactor, other methods must be considered as the conditions necessary for fusion of ^{8}Be are not often achievable by conventional means. Thus, for this aspect of the investigation, other reactions were considered which may provide a bridge between ^{8}Be and the CNO cycle.

Upon production, ^{8}Be begins decaying via alpha decay with a half life of 82as. This short interval can be accommodated by different means. The first: reaction rate modification introduced above. The other: composition of an alternative reaction chain which can compensate for the decay of ^{8}Be, described thusly. For this modified chain, the same reactions occur in the first steps, diverging after the production of ^{3}He and ^{3}H. These isomers are fused to produce ^{6}Li. Otherwise the reactions proceed identically according to the triple alpha process; fusing isotopes of helium to produce ^{7}Be, which is bombarded with neutron to produce ^{8}Be. At this point, the reactions split into two distinct branches. Upon decaying into ^{4}He nuclei, the branches proceed identically: the ^{6}Li fuses with alpha particles to produce ^{10}B and a photon. This is further bombarded with deuterons, to once again yield ^{12}C, which ignites two distinct CNO cycles within the reactor. This process is referred to as type II, and is illustrated in figure 2. These CNO cycles are each self-sustaining, again, contingent upon a steady supply of protium.

3.2 The Q-Value of Reactions

The q-values of the reactions for both reaction chains were observed to ensure that the reactions were all exothermic ($Q > 0$), or rather, that the sum of the q-values is > 0.

3.2.1 Type I

The q-values of the reactions in the consumption rate optimized chain were derived (*see figure 3*). These values were computed for reactions of single projectile and single target nuclei. Seeing as all of these reaction q-values met the > 0 criteria. This implies that assuming each of the reactions occur, they will produce energy. Because of this, the q-value of the reactions did not require further inquiry.

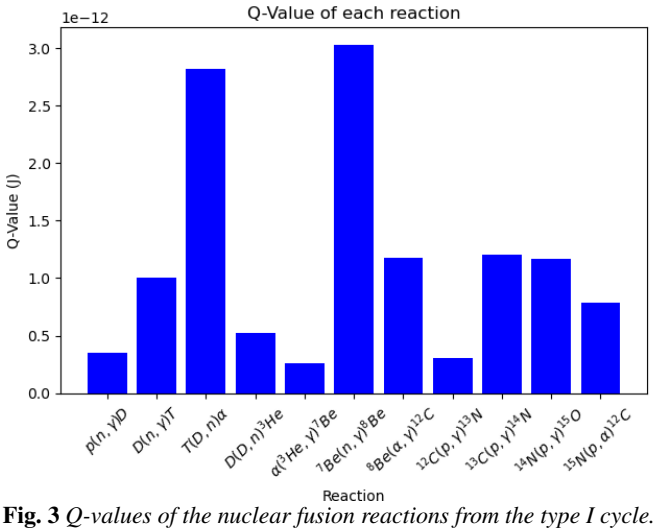

Fig. 3 *Q-values of the nuclear fusion reactions from the type I cycle. Original work of the author.*

3.2.2 Type II

The same process was applied to the type II reaction process, and the same information was gathered, that is, all of the reaction q-values met the > 0 criteria for exothermality. This data is shown in figure 4. From this, it becomes obvious that more energy is yielded by the type II reaction cycle than by the type I reaction cycle. This is due, in part to the greater quantity of matter-antimatter annihilations, discussed more later. Coincidentally, a peak can also be observed near the DT fusion,

which has already been demonstrated at NIF, however, this reaction is slightly exceeded by the bombardment of ^{7}Be with neutrons. After this reaction, the q-values level off, and remain approximately constant, with the exception of the ^{13}C(n,γ)^{14}N reaction.

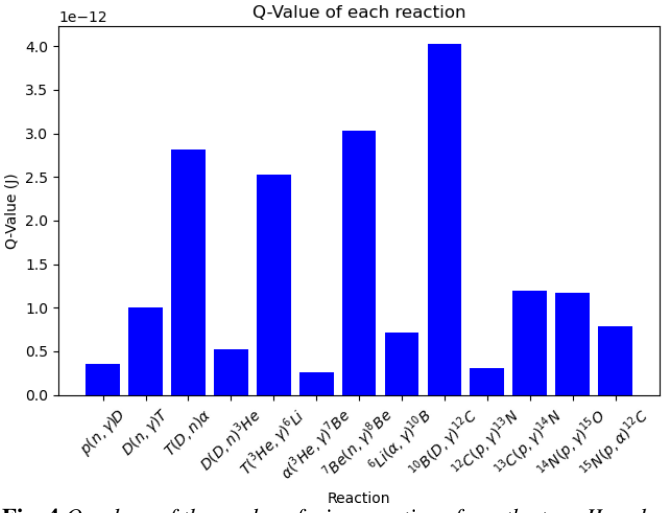

Fig. 4 *Q-values of the nuclear fusion reactions from the type II cycle. Original work of the author.*

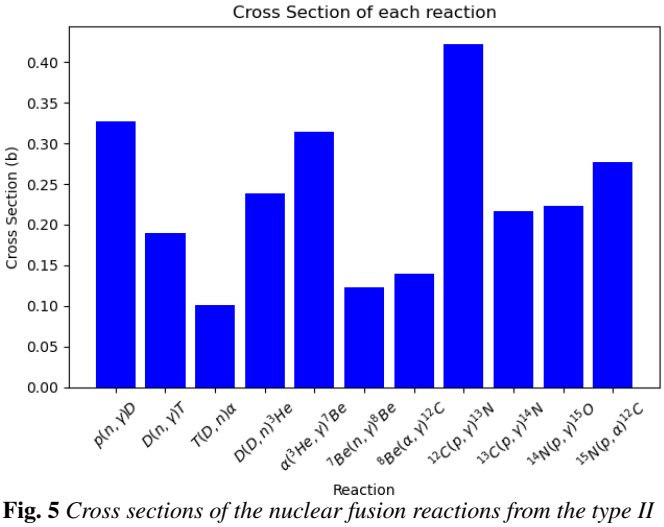

Fig. 5 *Cross sections of the nuclear fusion reactions from the type II cycle. Original work of the author.*

3.3 The Cross Section of Reaction

3.3.1 Type I

As stated above, nuclear cross section monitors the likelihood of the nuclear reaction occurring. The data computed for these reactions is shown in figure 5. These data demonstrate nuclear cross sections for each reaction which varies between 0.101b and 0.423b. These cross sections will be imperative later when investigating the rate of consumption. The cross sections of these reaction cross sections are consistent with the standard cross sections of nuclear cross sections for nuclear fusion reactions. These metrics are, however, limited in that they do not take into account the effects of nucleon-nucleon scattering, photoscattering, photodisintegration, and other quantum effects inside the suspended plasma.

3.3.2 Type II

Conversely, the reaction cross sectionslike the q-valuesare identical for certain reactions. The data found for these reactions are shown in figure 6. These data show a fluctuation in values between 0.101b and 0.509b. This reaction cycleunlike the type I reaction cycledoes not require the derivation of reaction rates. However, these cross sections are used in the computation of the Lawson criteria of a reactor below.

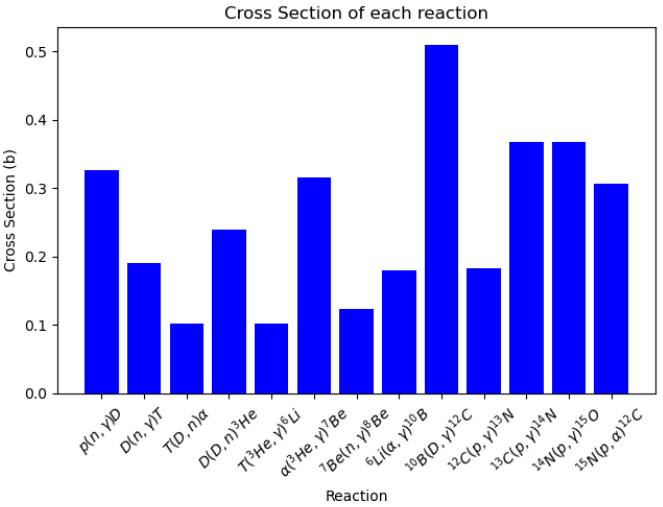

Fig. 6 *Cross sections of the nuclear fusion reactions from the type II cycle. Original work of the author.*

3.4 Maxwell-Boltzmann Analysis

3.4.1 Type I

For the reactions, Maxwell-Boltzmann diagrams were composed for the target reactants. These charts were produced using the equations described above. These charts served the purpose of computing the velocities of the particles. These values were in turn used to compute the temperatures required for the computation of the reaction rates. These Maxwell-Boltzmann diagrams for the type I reaction cycle are shown below in figure 7 (right).

These data show velocities of the order 10^5 m/s. As of now, the most commonly proposed method of energy extraction from a reaction is the boiling of water to turn a turbine. For this reason, these high number densities at high velocities are promising, as discussed below in the discussion.

These data were used to estimate the temperatures of each of the reactions. Because of this, the temperatures of each reaction were estimated just below the $3.63 \cdot 10^6$ K mark of the entire reaction chamber. The temperatures were furthermore related to the reduced masses of the temperatures in each reaction. This temperature data for the reactions in the type I reaction cycle is shown below in figure 7 (left).

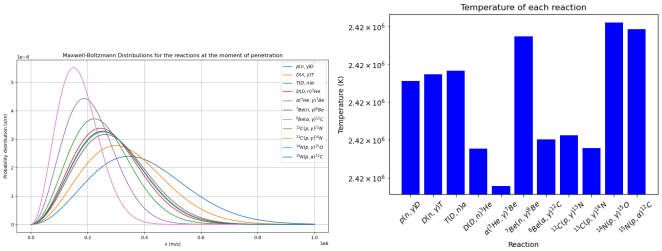

Fig. 7 *Left: Temperature data for the reaction in the type I reaction cycle. Right: Maxwell-Boltzmann diagrams of the nuclear fusion targets from the type I cycle. Original work of the author.*

3.4.2 Type II

This same process was applied to cycle II, and similar data was found. This consistency was attributed to the control temperature used in both surveys. The probability functions for the cycle II target nuclei are shown below in figure 8 (right).

These data show similar results to those of cycle I. Again, high number densities exist at high velocities: $\sim 10^5$, indicating a high temperature within the reactor vessel. This high temperature implies that the reactor could yield sufficient energy to generate wattage in a power facility.

These functions were used to exact the temperatures of the reactions. Using the methods described above to compute the temperatures of the reactions, the chart in figure 8 (left) was produced.

These temperatures all fell near below the original mark, for the same reason as the type I cycle.

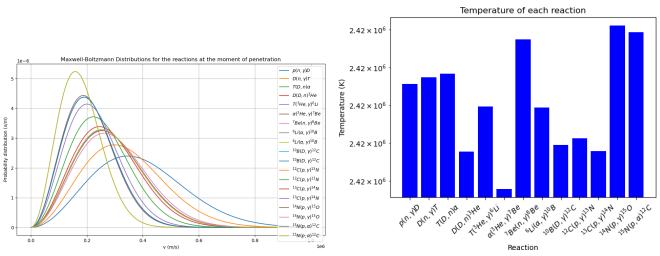

Fig. 8 *Left: Temperature data for the reaction in the type II reaction cycle. Right: Maxwell-Boltzmann diagrams of the nuclear fusion targets from the type II cycle. Original work of the author.*

3.5 Reaction Rate Analysis

3.5.1 Type I

Cross section-velocity average. Before the rate of molar consumption for the reactants could be derived, a set of averages between the cross sections and velocities needed to be computed. These values were derived from the average temperatures of the reactants shown in the Maxwell-Boltzmann diagrams. (*See figure 7*)

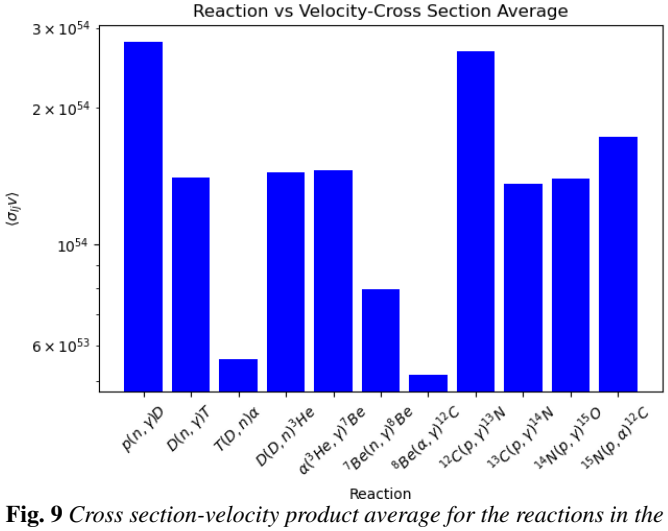

Fig. 9 *Cross section-velocity product average for the reactions in the type I reaction cycle. Original work of the author.*

Nuclear consumption rate. Based on the specifications of the cycle, certain criterion must be met to allow the cycle to occur. These are: $\dot{n}_I(^8\text{Be}) \geq 2.06 \cdot 10^{15}\text{mol/s}$, or $\dot{n}_I(^8\text{Be}) \geq \dot{n}_I(^7\text{Be})$. These criterion prompted this aspect of the study. Therefore, multiple mass flow rates of H_2 were tested. These mass flow rates were as follows: trigonometric ($\dot{m} = \sin^2 t$), polynomial ($\dot{m} = t^2 + t$), exponential ($\dot{m} = 2^{-t}$), and modified trigonometric ($\dot{m} = t \sin^2 t$). These functions produced the curves shown in figure 10.

The equations of nuclear consumption rate for the type I

reaction cycle are shown in Eqs. 25-34.

$$\frac{dn_I(\mathrm{p})}{dt} = -\langle\sigma_{\mathrm{R}1}v\rangle\frac{V\Phi_n}{v_n}\int_{[0,t]}\dot{m}_{\mathrm{H}_2}dt \tag{25}$$

$$\frac{dn_I(\mathrm{D})}{dt} = -\langle\sigma_{\mathrm{R}3}v\rangle\exp\left[\langle\sigma_{\mathrm{R}4}v\rangle(t-1)\right]\left[\int_{[0,t]}\frac{dn_I(\mathrm{p})}{dt}dt\right]^2 + \langle\sigma_{\mathrm{R}2}v\rangle\frac{V\Phi_n}{v_n}\int_{[0,t]}\frac{dn_I(\mathrm{p})}{dt}dt \tag{26}$$

$$\frac{dn_I(\mathrm{T})}{dt} = -\langle\sigma_{\mathrm{R}3}v\rangle\int_{[0,t]}\frac{dn_I(\mathrm{D})}{dt}dt\int_{[0,t]}\frac{dn_I(\mathrm{p})}{dt}dt \tag{27}$$

$$\frac{dn_I(\alpha)}{dt} = -\langle\sigma_{\mathrm{R}5}v\rangle\int_{[0,t]}\frac{dn_I(\mathrm{T})}{dt}dt\int_{[0,t]}\frac{dn_I(\mathrm{D})}{dt}dt - \langle\sigma_{\mathrm{R}7}v\rangle\int_{[0,t]}\frac{dn_I(^7\mathrm{Be})}{dt}dt\int_{[0,t]}\frac{dn_I(\mathrm{T})}{dt}dt \tag{28}$$

$$\frac{dn_I(^7\mathrm{Be})}{dt} = -\langle\sigma_{\mathrm{R}6}v\rangle\frac{V\Phi_n}{v_n}\int_{[0,t]}\frac{dn_I(\mathrm{T})}{dt}dt \tag{29}$$

$$\frac{dn_I(^8\mathrm{Be})}{dt} = -\langle\sigma_{\mathrm{R}7}v\rangle\int_{[0,t]}\frac{dn_I(^7\mathrm{Be})}{dt}dt\int_{[0,t]}\frac{dn_I(\mathrm{T})}{dt}dt \tag{30}$$

$$\frac{dn_I(^{12}\mathrm{C})}{dt} = -\langle\sigma_{\mathrm{R}8}v\rangle\int_{[0,t]}\frac{dn_I(^8\mathrm{Be})}{dt}dt\int_{[0,t]}\dot{m}_{\mathrm{H}_2}dt \tag{31}$$

$$\frac{dn_I(^{13}\mathrm{C})}{dt} = -\langle\sigma_{\mathrm{R}9}v\rangle\left(1-\left(\frac{1}{2}\right)^{\frac{t}{t_{1/2}(^{13}\mathrm{N})}}\right) \times\int_{[0,t]}\frac{dn_I(^{12}\mathrm{C})}{dt}dt\int_{[0,t]}\dot{m}_{\mathrm{H}_2}dt \tag{32}$$

$$\frac{dn_I(^{14}\mathrm{N})}{dt} = -\langle\sigma_{\mathrm{R}10}v\rangle\int_{[0,t]}\frac{dn_I(^{13}\mathrm{C})}{dt}dt\int_{[0,t]}\dot{m}_{\mathrm{H}_2}dt \tag{33}$$

$$\frac{dn_I(^{15}\mathrm{N})}{dt} = -\langle\sigma_{\mathrm{R}11}v\rangle\left(1-\left(\frac{1}{2}\right)^{\frac{t}{t_{1/2}(^{15}\mathrm{O})}}\right) \times\int_{[0,t]}\frac{dn_I(^{14}\mathrm{N})}{dt}dt\int_{[0,t]}\dot{m}_{\mathrm{H}_2}dt \tag{34}$$

These equations were composed based on the different reactions they are consumed in, that is, if a reactant is used in multiple reactions, the consumption rates for both reactions were added together. Furthermore, the coefficient $1-0.5^{\frac{t}{t_{1/2}}}$, is used in some of these definitions. This coefficient is added to account for the delay in the production of sufficient quantities of reactant from radioactive decay of the products of the previous reaction.

The functions shown in figure 10 can be extrapolated out to $\dot{n}_I(^8\mathrm{Be})$. It is clear from the graph that reaction rates increase for each reaction. It then follows that because $\dot{n}_I(\mathrm{p})$ clears the $1.22\cdot10^6$ mol/s threshold, $\dot{n}_I(^8\mathrm{Be})$ too should meet this criteria. Implications of this will be discussed later. These functions may also be converted into their corresponding signals using the Fourier inversion theorem [15].

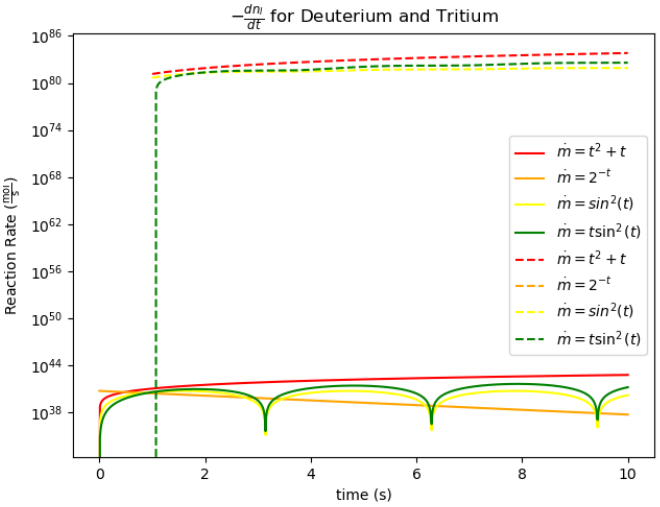

Fig. 10 *Rate of nuclear consumption for the type I reaction cycle. Original work of the author.*

These functions require peak temperatures north of 2.4MK. Temperatures achieved in the NIF experiment were in the range of 13.1 ± 0.7eV for DT fusion and 12 ± 1eV for DD fusion. This indicates a peak recorded temperature of 13.8eV, which converts to approximately 0.16MK. However, the laser pulse was able to achieved peak temperature of 300eV, which is equivalent to 3.48MK[?]. This peak temperature–if sustained–would be sufficient to ignite the CNO-I cycle, and furthermore suffice the temperature parameter of the equations demonstrated for Eqs. 23-32.

Given the specifications of this computation, and accepted theory on branch III of the pp-chain[?], protons are able to tunnel beyond the Coulomb barrier and fuse with the ^{7}Be nucleus. This provides the quantum mechanical justification of the solution, and thus resolves that issue with the type I reaction cycle.

3.5.2 Type II

The consumption rate of the reactants was not pertinent to show the viability of this fusion cycle and was therefore omitted from this inquiry.

3.6 Gamow Peaks

3.6.1 Type I

From this aspect of the experiment, data was gathered to show the relation between cross section and probability of reaction. This relation is shown in figure 11.

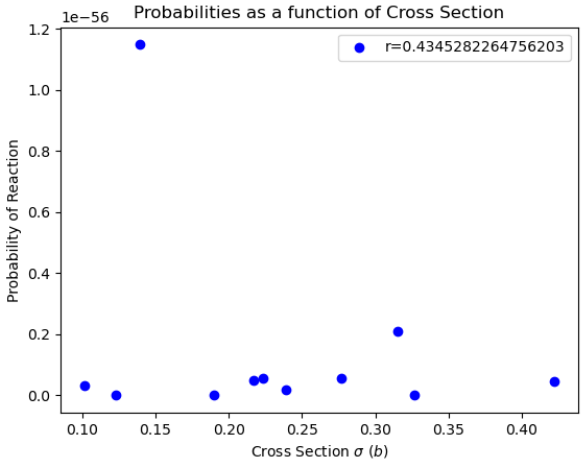

Fig. 11 *Probabilities of reaction for the type I cycle shown with respect to reaction cross section.* Original work of the author.

These probabilities are exceedingly low due to the temperature of the reactions and the conditions that have been achieved via artificial means. The probabilities represent the proportion of particles traveling at the necessary velocity derived above. Because of this, increases in $f(v_{\mathrm{rxn}})$ of each reaction are necessary. Methods of achieving this are discussed later.

Furthermore, the Pearson r coefficient demonstrates a moderate correlation between σ and $f(v_{\mathrm{rxn}})$ with $r \approx 0.434$. This correlation is likely due to the fact that both functions $\propto \exp Z_I Z_j$. This proportionality could furthermore contribute to a solution to the temperature problem, discussed further below.

3.6.2 Type II

Again, data from this experiment were gathered and related to the cross section in the figure below.

Likewise, the probabilities for these reactions was exceedingly low, and thus require further improvement beyond the scope of this paper. These reactions may be enabled via increased temperature, similar to the reaction in the type I cycle.

A much stronger correlation was observed between σ and $f(v_{\mathrm{rxn}})$ than in the previous example, $r \approx 0.819$. This correlation can also be used as an instrument for improving the probability.

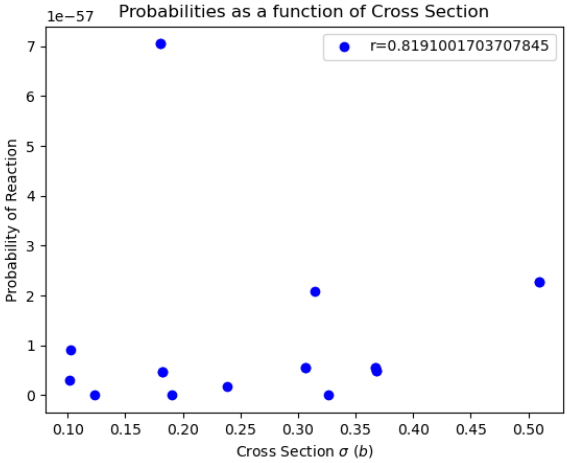

Fig. 12 *Probabilities of reaction for the type II cycle shown with respect to reaction cross section.* Original work of the author.

4 Discussion

4.1 Correlations in Q-value and Cross Section

For both the type I and type II reaction cycles, strong correlation was noticed between the q-value and cross sections of the reactions. Furthermore, reactions from the CNO cycles tended to have higher q-values, demonstrating their necessity in future experiments.

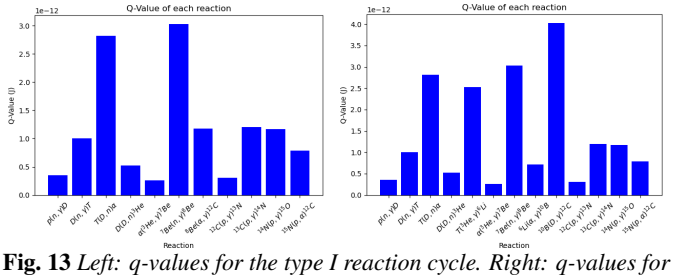

Fig. 13 *Left: q-values for the type I reaction cycle. Right: q-values for the type II reaction cycle. Original work of the author.*

4.1.1 Type I

For the type I reaction cycle, the correlations between the q-value of reaction and cross section of reaction may be seen in two charts: with each value plotted as a function of the stage, and in a scatterplot (*see figure 14*).

4.1.2 The ^{7}Be(n,γ)^{8}Be Special Case

The calculated value of the cross section of reaction for the ^{7}Be(n,γ)^{8}Be reaction are similar, however, the computed value for σ is greater than the experimental value at $Q = 18.89$eV retrieved from the JENDL-5 database [16]. The experimntal value $\sigma_{\mathrm{exp}} \approx 5.6$mb, where as the calculated value $\sigma_{\mathrm{calc}} \approx 123$mb. This major discrepancy can be accounted for by the conditions

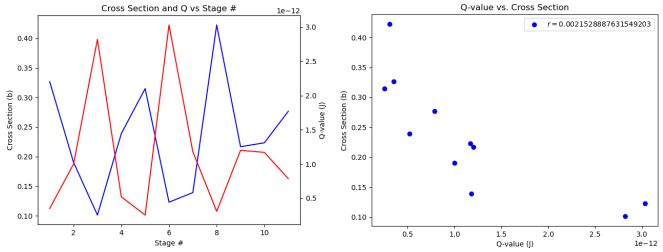

Fig. 14 *Left: Q-values and cross sections of each reaction stage in the type I cycle. Right: Q-values and cross sections of reactions in the type I cycle scattered. Original work of the author.*

assumed for the reaction cycle. Differences in the experimental method used in the JENDL-5 experiment and those assumed in this computation should sufficiently account for this discrepancy.

4.1.3 Type II

For the type II reaction cycle, similar correlation can be observed, and the same plots were composed for these reactions (*see figure 15*). The correlation for the type II reaction cycle is ≈ 0.276, whereas the correlation coefficient of the type I reaction cycle is ≈ 0.002.

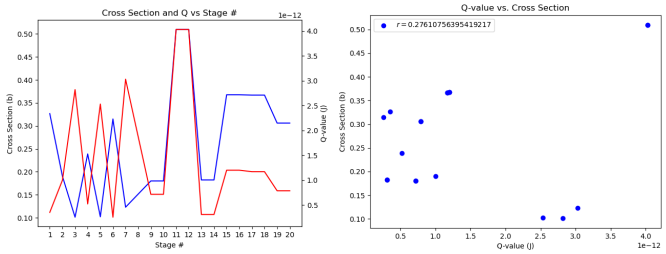

Fig. 15 *Left: Q-values and cross sections of each reaction stage in the type II cycle. Right: Q-values and cross sections of reactions in the type II cycle scattered. Original work of the author.*

4.1.4 Improvements to the Probability of Reaction

As discussed above, for both the type I and type II cycles, the Gamow peaks fall far below the reasonable threshold for nuclear fusion to occur given the specifications of existing experiments. In these cases, reactions are suppressed by coulomb repulsion, indicating that the nuclei do not achieve close enough proximity for the strong nuclear force to prevail.

Discussed in the findings was the proportional nature of both σ and $f(v_{\mathtt{rxn}})$. That is, both σ and $f(v_{\mathtt{rxn}}) \propto \exp(Z_I Z_j)$. Although this relation exists, its viability as a means of improving reaction probability disintegrates when we consider the fact that Z_I and Z_j are fixed for all reactions. However, improvements made to the heating mechanism of the reactor could also provide means for improving the reaction probability. Increasing pulse duration allows for the reactor to achieve a higher peak temperature, thus increasing that variable in the equation. However, a key specification of this reactor is that the peak temperature must not exceed the melting point of the container material. Therefore, future investigations may incorporate heating elements like induction heaters and nuclear fission stages as a means of heating reactants, without melting the container.

4.1.5 Lawson Criteria

Across various fusion experiments, the Lawson criteria[17] has been a key factor in determining fusion ignition. It has undergone development with time and the most recent figure, used by NIF, is:

$$\mathtt{GLC}_{\mathtt{H}} = P_{\mathtt{peak}}\,\tau H(T) \tag{35}$$

Where $P_{\mathtt{peak}}$ is the peak temperature achieved in the experiment, τ is the confinement time, and $H(T)$ is a complicated function of energy and temperature. However, reliability of this figure may not hold for reactions which provide reactants for subsequent reactions, as well as cycles which form closed loops (like the CNO). Thus, an improved model for the Lawson criteria is necessary to gauge fusion ignition. This new model should take into account for the fueling of subsequent reactions, as well as utility of products in multiple reactions.

4.1.6 Reactor Efficiency

Values describing the input and output energies of the reactor have already been composed and used in other experiments. This is the target gain:

$$G_{\mathtt{target}} = \frac{E_{\mathtt{out}}}{E_{\mathtt{in}}} \tag{36}$$

and has been used as the basis for fusion ignition (i.e. $G_{\mathtt{target}} > 1$ indicating ignition). While this works well to describe the efficiency of the system as a whole, it breaks down in describing the efficiency of individual steps. Future experiments could use the rates of nuclear consumption of a given reaction and of the next reaction as a measure of efficiency of the base reaction:

$$\eta_{\mathtt{reactor}} = \frac{\dot{n}_I(\mathtt{RX})}{\dot{n}_I(\mathtt{RX{+}1})} = \frac{\dot{n}_I(\mathtt{RX{-}1})}{\dot{n}_I(\mathtt{RX})}. \tag{37}$$

In this instance, $\eta_{\mathtt{reactor}}$ is the efficiency of the reactor, and should not be confused with η from earlier, the charge dependence of nuclear cross section. Furthermore, `RX-1`, `RX`, `RX+1` denote the reaction rates of a preceding reaction (`RX-1`), base reaction (`RX`), and a subsequent reaction (`RX+1`).

4.2 Looking Forward

Before these reactions may be deployed in the energy grid, a series of laboratory experiments similar to NIF are necessary to prove these extended cycles in concept. Because of the relatively low temperature and pressures required to fuse hydrogen, DT and DD fusion reactions have been the aim of laboratories until now. However, now that DD and DT fusion have achieved target

gains greater than unity[?], reactions of heavier elements may commence to fill the remaining gap. Similar to the N221204 shot, a target should be composed which includes a DT core, but should also incorporate the other intermediates such as nitrogen, oxygen, etc. For this reason, the cryogenic DT mantle held between the HDC ablator shell and the DT gaseous volume could be replaced with noble gas compounds, amines, cyanides, water, etc. and other molecular groups at varying proportions to derive an optimal fuel pellet. These derivations are critical to the proof of these fusion cycles.

Conversely, a key aspect of both reaction cycles. is the emission of positrons: antiparticle counterparts of the electron. These antileptons interact with matter particles, namely, the down quark: abundant inside hadrons (protons and neutrons, free inside the plasma), and the electron: suspended freely inside a plasma. These free positrons interact with negatively charged particles in two cases.

$e^+(e^-,\gamma)\gamma$ Annihilation. Matter-antimatter annihilation has been studied very rigorously, and the nature of these interactions is very well known. Upon collision, electrons and positrons yield a pair of photons at high energies. The photons are in the gamma range, and often interact with other matter, through methods like pair production, photofission, and other scattering modes.

$d(e^+,\nu_e)u$ Annihilation. Conversely, other interactions can occur in which positrons annihilate with down quarks. Preserving the necessary values (spin, charge, etc.), it can be easily derived that this interaction yields a neutrino and an up quark. Because of these effects, the efficiency of these reactions may be undercut, and therefore, bears the weight of further investigation. The chaotic effects of these interactions are difficult to monitor and must therefore be examined experimentally, and could also be used as a benchmark to determine the efficacy of the reaction cycles.

These interactions and their chaos could also see application as the excess photons contribute to the total energy evolved from the cycles. Furthermore, any subsequent experiments should examine methods by which the scattering and annihilation effects may be minimized inside the reactor vessel.

4.3 Applications

The burnup times of these reaction cycles are vastly different, and so too are the quantities of photons that the cycles produce. This difference gives rise to a diverse set of applications.

Conversely, the discoveries already made at NIF[?] proved the framework for a CNO-scaffolded approach to fusion power. Using a similar experimental framework[18] and a slight variation of the fuel structure to incorporate more complex molecules like noble gas compounds, amines, cyanides, water, etc. Furthermore, by extending the pulse duration of an indirect drive ICF reactor, reactants may achieve a higher temperature, while the energy required to power this extension can be subsidized by the higher q-values of the reactions. Given these new specifications, heat and kinetic energy of these particles from the DT and DD reactions would be sufficient to ignite a triple alpha process, and develop into a CNO cycle.

4.3.1 Type I

The burnup time of the type I cycle is much less than that of the type II cycle, and this is due to the accelerated nature of the rates of nuclear consumption that is required for the direct consumption of ^{8}Be. However, a full execution of this reaction cycle will yield 7.6TJ of energy per mole of reactant. Taking into account a burn-up fraction $= 10^{-5}\rho RT^{n-0.5} \approx 0.157$ (ρ, R, T being experimental values from the NIF experiment)[?], this figure is actually nearer 1.2TJ. This high energy and short time span implies a very high power.

The high power nature of the type I reaction cycle makes this reaction cycle much better suited for remote environments. As the demand for independent energy in space, that is, power for a spacecraft produced entirely independent from reserves, the type I cycle should see consideration for its relatively safe nature, as well as for its brief tenure. This cycle is also very well suited for modular designs: small-scale operations which need only last a few years with few to no refueling operations.

Other applications also arise when considering the more nefarious deployments of nuclear fusion: weaponry. Gadgets produced during the Manhattan project hypothesized by Teller, Ulam, and Von Neuman[18] successfully demonstrated a thermonuclear reaction: nuclear fusion reactions ignited via compression by a nuclear fission stage. Using these preliminary findings in tandem with the framework of the type I reaction cycle, hostile actors may be inclined to develop more powerful weapons on this platform. Although, more optimistically, this hybrid nuclear research may also give rise to highly efficient hybrid nuclear plants.

4.3.2 Type II

In contrast, the type II reaction cycle has a much larger burnup time. Because of this, the type II reaction cycle would have a similar wattage capacity–the amount of power the reaction cycle is capable of producing. This similarity occurs because of the proportionally large energy and tenure relative to the type I reaction cycle.

This comparative power also suggests an ability for nuclear fusion fuels to be implemented into a nuclear fission fuel matrix. The NIF demonstration used a fuel pellet with a diameter of approximately 2mm[??]. Future applications of this type II cycle could integrate fusion fuel pellets similar to those from the N221204 and N210808 into a nuclear fission reactor. Doing so would provide the high number density of neutrons for the primordial bombardment reactions, as well as the necessary radioactive conditions to ionize the reactants, suspending them in plasma.

This cycle is particularly well-suited for large-scale applications where longevity and permanence are paramount. It aligns with the model of conventional power plants, such as the coal and nuclear facilities still in operation today. Additionally, the inherently high power output of this reactor type necessitates continuous monitoring to ensure it remains within a safe, exothermic regime. Overall, when considering reaction chains intended to sustain cities and towns, this cycle emerges as the superior candidate of the two.

5 Acknowledgments

I would like to thank my research mentorsMrs. Kasper, Mrs. Reier, Mrs. Marcus, Mr. Hedrick, and Mrs. Konradt-as well as my past science and mathematics teachers for their guidance and support throughout these experiments. I am also grateful to my familymy mothers, Cheryl King and Julie Hall; my grandparents, Gail and Ronald King†; and my brothers, who have been like family–in every way that matters-for their constant encouragement.

References

1 H. Abu-Shawareb, R. Acree, P. Adams *et al.*, *Physical Review Letters*, 2024, **132**, year.

2 H. Bethe, *The fusion hybrid*, `http://large.stanford.edu/publications/coal/references/docs/bethe.pdf`, 1979.

3 H. Bethe, *Physical Review*, 1939, **55**, 103–103.

4 A. S. Eddington, *The Scientific Monthly*, 1920, **11**, 297–303.

5 C. von Weizsäcker, *The Biographical Encyclopedia of Astronomers*, 1938, vol. 38, pp. 633–646.

6 C. von Weizsäcker, *The Biographical Encyclopedia of Astronomers*, 1937, vol. 38, pp. 176–191.

7 P. Virtanen, R. Gommers, T. E. Oliphant *et al.*, *Nature Methods*, 2020, **17**, 261–272.

8 E. Adelberger, A. García, R. Robertson *et al.*, *Solar fusion cross sections II: The pp chain and CNO cycles*, `https://arxiv.org/pdf/1004.2318`, 2010.

9 E. Teller, S. Ulam and J. V. Neumann, *On heterocatalytic detonations I: Hydrodynamic lenses and radiation mirrors*, Los alamos national laboratory technical report, 1951.

10 L. Siess, M. Livio and J. Lattanzio, *Structure, evolution, and nucleosynthesis of primordial stars*, ArXiv preprint, 2002.

11 A. Einstein, *On the electrodynamics of moving bodies*, `https://www.fourmilab.ch/etexts/einstein/specrel/specrel.pdf`, 1905.

12 D. D. Clayton, *Principles of Stellar Evolution and Nucleosynthesis*, University of Chicago Press, 2007.

13 D. Newell and E. Tiesinga, *NIST Special Publication 330: The International System of Units*, National institute of science and technology technical report, 2019.

14 R. Alpher, H. Bethe and G. Gamow, *Physical Review*, 1947, **73**, 803.

15 G. Folland, *Fourier Analysis and Its Applications*, American Mathematical Society, 2009.

16 M. Chadwick, M. Herman, P. Oblozinsky *et al.*, *Nuclear Data Sheets*, 2011, **112**, 2887–2996.

17 J. D. Lawson, *Proceedings of the Physical Society. Section B*, 1957, **70**, 6–10.

18 M. Agostini, K. Altenmuller, S. Appel *et al.*, *Nature*, 2020, **587**, 577–582.

Appendix A

Code used to derive the data shown below.

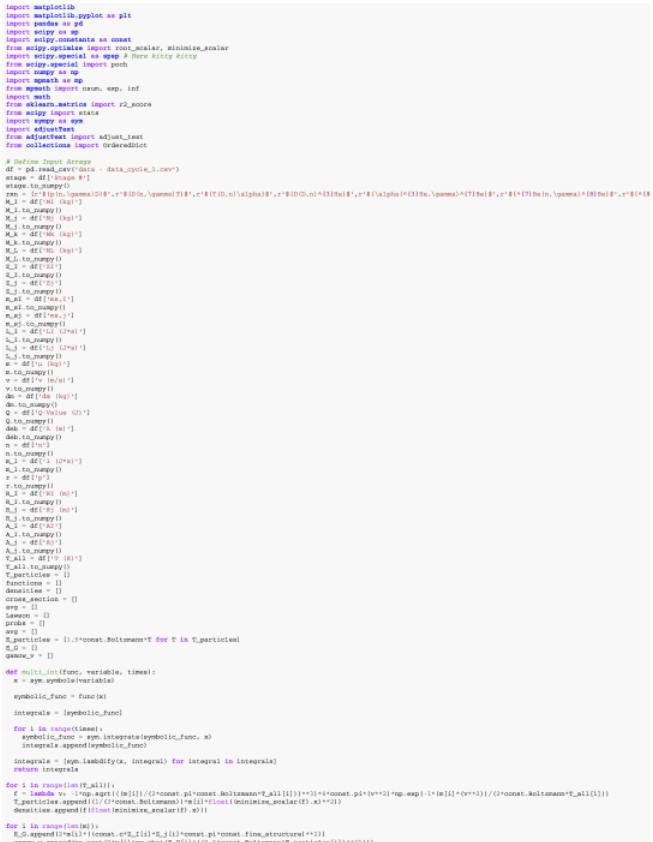

```
import matplotlib
import matplotlib.pyplot as plt
import pandas as pd
import scipy as sp
import scipy.constants as const
from scipy.optimize import root_scalar, minimize_scalar
import scipy.special as spsp # Here kitty kitty
from scipy.special import perh
import numpy as np
import mpmath as mp
from mpmath import nsum, exp, inf
import math
from sklearn.metrics import r2_score
from scipy import stats
import sympy as syn
import adjustText
from adjustText import adjust_text
from collections import OrderedDict

# Define Input Arrays
df = pd.read_csv('data - data_cycle_1.csv')
stage = df['Stage #']
stage.to_numpy()
rxn = [r'$p(n,\gamma)2D$',r'$^{D(n,\gamma)^{3}He$',r'$^{D(D,n)^{3}He$',r'$^{\alpha(^{3}He,\gamma)^{7}Be$',r'$^{\alpha(^{3}He,\gamma)^{7}Be(e^-,\gamma)^{7}Li$',r'$^{\alpha(^{7}Be(n,\gamma)^{8}Be$',r'$^{\alpha(^{7}Be(n,\gamma)^{8}Be(e^-,\gamma)^{8}Li$',r'$^{\alpha(^{7}Be(n,\gamma)^{8}Be(e^-,\gamma)^{8}Li(e^-,\gamma)^{8}Be$',r'$^{\alpha(^{7}Be(n,\gamma)^{8}Be(e^-,\gamma)^{8}Li(e^-,\gamma)^{8}Be(e^-,\gamma)^{8}Li(e^-,\gamma)^{8}Be$']
M_1 = df['M1 (kg)']
M_1.to_numpy()
M_2 = df['M2 (kg)']
M_2.to_numpy()
M_3 = df['M3 (kg)']
M_3.to_numpy()
M_4 = df['M4 (kg)']
M_4.to_numpy()
M_5 = df['M5 (kg)']
M_5.to_numpy()
X_1 = df['X1']
X_1.to_numpy()
X_2 = df['X2']
X_2.to_numpy()
X_3 = df['X3']
X_3.to_numpy()
m_e1 = df['me_1']
m_e1.to_numpy()
m_e2 = df['me_2']
m_e2.to_numpy()
L_1 = df['L1 L2*e1']
L_1.to_numpy()
L_2 = df['L2 L2*e2']
L_2.to_numpy()
m = df['m (kg)']
m.to_numpy()
v = df['v (m/s)']
v.to_numpy()
dm = df['dm (kg)']
dm.to_numpy()
Q = df['Q-Value (J)']
Q.to_numpy()
deb = df['E_b (e)']
deb.to_numpy()
n = df['n']
n.to_numpy()
e_1 = df['1 L2*e1']
e_1.to_numpy()
r = df['p']
r.to_numpy()
E_1 = df['E1 (m)']
E_1.to_numpy()
E_2 = df['E2 (m)']
E_2.to_numpy()
A_1 = df['A1']
A_1.to_numpy()
A_2 = df['A2']
A_2.to_numpy()
T_all = df['T (K)']
T_all.to_numpy()
T_particles = []
functions = []
densities = []
cross_section = []
avg = []
Lawson = []
probs = []
avg = []
E_particles = [1.5*const.Boltzmann*T for T in T_particles]
E_G = []
gamow_y = []

def multi_int(func, variable, times):
  x = syn.symbols(variable)

  symbolic_func = func(x)

  integrals = [symbolic_func]

  for i in range(times):
    symbolic_func = syn.integrate(symbolic_func, x)
    integrals.append(symbolic_func)

  integrals = [syn.lambdify(x, integral) for integral in integrals]
  return integrals

for i in range(len(T_all)):
  f = lambda v: -1*np.sqrt((m[i])/(2*const.pi*const.Boltzmann*T_all[i]))**3)*4*const.pi*(v**2)*np.exp(-1*(m[i]*(v**2))/(2*const.Boltzmann*T_all[i]))
  T_particles.append((1/3)*const.Boltzmann)*m[i]*float(minimize_scalar(f).x)**2)
  densities.append(f(float(minimize_scalar(f).x)))

for i in range(len(m)):
  E_G.append(2*m[i]*(const.c*Z_1[i]*Z_2[i]*const.pi*const.fine_structure)**2)
  gamow_y.append(np.sqrt(2*m[i]*np.cbrt(E_G[i])*(0.5*const.Boltzmann*T_particles[i])**2))

for i in range(len(T_all)):
```

Fig. 16 Code Used to derive figures for the type I reaction cycle. Original work of the author.

Fig. 17 Code Used to derive figures for the type II reaction cycle. Original work of the author.

Appendix B

Input data formulae shown in Eqs. 33-35.

$$\mu = \frac{m_I m_j}{m_I + m_j} \tag{38}$$

$$\eta = \frac{Z_I Z_j e^2}{\hbar v} \tag{39}$$

$$\rho = R_I \sqrt{\frac{2\mu Q}{\hbar^2}} \tag{40}$$

Natural Constants shown in tables 1-2.

Stage	Reaction	m_I (10^{-26} kg)	m_j (10^{-26} kg)	Z_I	Z_j	R_I (10^{-15} m)	R_j (10^{-15} m)	A_I	A_j
1	p(n,γ)D	0.167	0.168	1	0	1.2	1.2	1	1
2	D(n,γ)T	0.335	0.168	1	0	1.51	1.51	2	1
3	T(D,n)α	0.501	0.335	1	1	1.73	1.51	3	2
4	D(D,n)^{3}He	0.335	0.335	1	1	1.51	1.51	2	2
5	α(^{3}He,γ)^{7}Be	0.665	0.501	2	2	1.90	1.73	3	4
6	^{7}Be(n,γ)^{8}Be	1.17	0.168	4	0	2.30	1.20	7	1
7	^{8}Be(α,γ)^{12}C	1.33	0.665	4	2	2.40	1.90	8	4
8	^{12}C(p,γ)^{13}N	1.99	0.167	6	1	2.70	1.2	12	1
9	^{13}C(p,γ)^{14}N	2.16	0.167	6	1	2.81	1.2	13	1
10	^{14}N(p,γ)^{15}O	2.33	0.167	7	1	2.89	1.20	14	1
11	^{15}N(p,α)^{12}C	2.49	0.167	7	1	2.96	1.2	15	1

Table 1 Input data for the type I reaction cycle

Stage	Reaction	m_I (10^{-26} kg)	m_j (10^{-26} kg)	Z_I	Z_j	R_I (10^{-15} m)	R_j (10^{-15} m)	A_I	A_j
1	p(n,γ)D	0.167	0.168	1	0	1.2	1.2	1	1
2	D(n,γ)T	0.335	0.168	1	0	1.51	1.51	2	1
3	T(D,n)α	0.501	0.335	1	1	1.73	1.51	3	2
4	D(D,n)^{3}He	0.335	0.335	1	1	1.51	1.51	2	2
5	T(^{3}He,γ)^{6}Li	0.501	0.501	1	2	1.73	1.73	3	3
6	α(^{3}He,γ)^{7}Be	0.665	0.501	2	2	1.90	1.73	3	4
7	^{7}Be(n,γ)^{8}Be	1.17	0.168	4	0	2.30	1.20	7	1
8,9	^{6}Li(α,γ)^{10}B	0.999	0.665	3	2	2.18	1.90	6	4
10,11	^{10}B(D,γ)^{12}C	1.66	0.335	5	1	2.59	1.51	10	2
12,13	^{12}C(p,γ)^{13}N	1.99	0.167	6	1	2.70	1.2	12	1
14,15	^{13}C(p,γ)^{14}N	2.16	0.167	6	1	2.81	1.2	13	1
16,17	^{14}N(p,γ)^{15}O	2.33	0.167	7	1	2.89	1.20	14	1
18,19	^{15}N(p,α)^{12}C	2.49	0.167	7	1	2.96	1.2	15	1

Table 2 Input data for the type II reaction cycle